

www.acsanm.org Article

# Factors Controlling Intercalation of Metal Atoms into WS<sub>2</sub>: Implications for Electronically Tunable Semiconductors

Kuixin Zhu, Yiyin Tao, Sagarmoy Mandal, Ming Chen, and Christina W. Li\*



Cite This: ACS Appl. Nano Mater. 2023, 6, 16846-16855



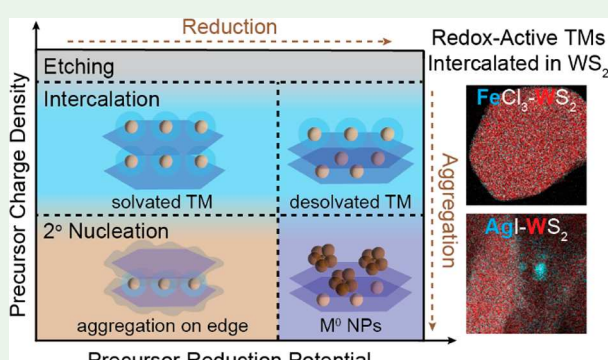
ACCESS I

Metrics & More

Article Recommendations

Supporting Information

ABSTRACT: The ability to tune the carrier transport properties of semiconducting two-dimensional materials is critical toward their eventual integration into nanoelectronic devices. Intercalation of transition-metal atoms and complexes into the interlayer galleries of two-dimensional transition-metal dichalcogenides (TMDs) can have a significant impact on the electronic structure and transport properties of the host material. However, because of the redox lability of transition metals, the intercalation process is frequently accompanied by undesired side reactions, including secondary nucleation, reduction, and degradation. In this work, we perform a systematic study on the intercalation of transition-metal cations into lithiated WS<sub>2</sub> (Li<sub>x</sub>WS<sub>2</sub>) in order to elucidate synthetic and structural design rules for achieving selective intercalation over secondary nucleation. We show that the



Precursor Reduction Potential

intercalation process, driven by charge transfer and electrostatic interactions, can be controlled by tuning the charge density and reducibility of the transition-metal precursor complex. For less reducible precursors, a higher charge density enables a stronger interaction between the cation and the anionic WS2 sheet, resulting in intercalation of solvated ions with no secondary nucleation of metal oxide nanoparticles. For more reducible cations, reduction and desolvation of the precursor complex occur first followed by zerovalent intercalation of the desolvated atom. Kelvin probe force microscopy measurements show that intercalated metal ions raise the Fermi level of WS2 by up to 90 meV compared to the LixWS2 precursor, resulting in improvements in both the conductivity and carrier activation energy.

KEYWORDS: transition-metal dichalcogenides, tungsten disulfide, layered materials, intercalation, conductivity, work function

## INTRODUCTION

Semiconducting two-dimensional materials are promising candidates for incorporation into next-generation nanoelectronic devices, but systematically tuning their carrier density and mobility remains a significant challenge compared to conventional semiconductors such as silicon. <sup>1-4</sup> A critical strategy toward tuning the electronic, 5-8 optical, 9-11 and magnetic 12,13 properties of these materials is through intercalation of guest atoms into the interlayer galleries of the two-dimensional sheets. <sup>14–19</sup> In most cases, the intercalation process is driven by charge transfer from the intercalant atom<sup>20-23</sup> or an external reducing potential<sup>24,25</sup> to the conduction band of the host material. Group VI (Mo, W) transition-metal dichalcogenides (TMDs) show great promise for nanoelectronic applications, 26 but their high energy conduction band limits intercalants to those that are stable under strongly reducing conditions or are themselves highly reducing. 17,27,28

As an alternative to direct charge-transfer intercalation, guest species can also be introduced in a stepwise fashion, where charge transfer is initiated using an alkali metal reductant and subsequent exfoliation-restacking enables incorporation of a more diverse slate of molecular intercalants. 29-34 This method generally results in disordered intercalant species that do not interact strongly with the TMD basal planes and exert a weak electronic influence. Recently, our group showed that V<sup>2/3+</sup> molecular complexes can be intercalated into WS2 using a modified two-step process: charge-transfer intercalation of Li<sup>+</sup> using *n*-butyllithium (*n*-BuLi) followed immediately by cationexchange to the redox-active V<sup>3+</sup> species.<sup>35</sup> Unlike alkali ions, the d-orbitals of intercalated V complexes are able to hybridize with the WS<sub>2</sub> conduction band and modulate the work function and electronic properties of the TMD.

In order to further improve the carrier transport properties of WS2, we wanted to explore the intercalation of other redoxactive transition-metal (TM) ions besides vanadium that could exhibit even stronger hybridization to the WS<sub>2</sub> basal planes. A

Received: July 3, 2023 Accepted: August 29, 2023 Published: September 8, 2023





major challenge with the intercalation of redox-active TMs is their tendency to secondary nucleate and/or reduce in the presence of the lithiated TMD, as has been previously shown with the formation of  $\mathrm{Co(OH)_2}^{36}$  and noble metal (Pt, Ru, Pd, Au)<sup>37</sup> nanoparticles intercalated in  $\mathrm{MoS_2}$ . As such, our first goal was to develop a general mechanistic understanding of the cation-exchange reaction between transition-metal ions and lithiated  $\mathrm{WS_2}$  in order to achieve selective intercalation. In this work, we study an array of transition-metal precursors with varying charge densities, reduction potentials, ionic radii, and oxidation states and elucidate synthetic rules for achieving selective intercalation relative to undesired competitive processes: secondary nucleation and degradation.

#### EXPERIMENTAL SECTION

**Synthesis of Li<sub>x</sub>WS<sub>2</sub>.** The lithiation of bulk WS<sub>2</sub> is based on a literature procedure. To a 25 mL three-neck round-bottom flask containing solid tungsten disulfide (300 mg, 1.2 mmol, 1.0 equiv) was added 1.6 M n-butyllithium in hexanes solution (3 mL, 4.8 mmol, 4.0 equiv). The n-butyllithium solution was diluted to 0.53 M with 6 mL of degassed cyclohexane. The solution was then refluxed at 75 °C under N<sub>2</sub> atmosphere for 48 h. After reaction, the solid product was recovered by centrifugation at 8500 rpm for 1 min and washed with hexanes three times under N<sub>2</sub> atmosphere.

Synthesis of TM-Intercalated  $\overline{WS_2}$ . Li<sub>x</sub>WS<sub>2</sub> (50 mg, 0.20 mmol, 1.0 equiv) was suspended in an NMF solution (5 mL) containing transition-metal halide precursor (0.40 mmol, 2.0 equiv), and the mixture was stirred at room temperature under N<sub>2</sub> atmosphere for 1 h. After reaction, the products were isolated from the precursor solution by centrifugation at 8700 rpm for 5 min. The solid was rinsed with additional NMF (10 mL) three times or until the supernatant was completely colorless. Then, THF (5 mL) and hexanes (2 mL) were added to remove residual NMF solvent in the sample, and the solid was recovered by centrifugation at 8700 rpm for 5 min. This process was repeated one time to ensure complete removal of NMF prior to drying under vacuum. Additional information about each category of transition-metal precursor is provided below.

VCl<sub>3</sub>, CrCl<sub>2</sub>, CrCl<sub>3</sub>·6H<sub>2</sub>O, MnCl<sub>2</sub>·6H<sub>2</sub>O, FeCl<sub>2</sub>, FeCl<sub>3</sub>, CoCl<sub>2</sub>, NiCl<sub>2</sub>, ZnCl<sub>2</sub>·6H<sub>2</sub>O, GaCl<sub>3</sub>, InCl<sub>3</sub>. Significant unreacted transition-metal precursor remains in the supernatant after the reaction, and the color of the supernatant during cleaning matches that of the precursor.

CuCl, CuCl<sub>2</sub>, Agl. The supernatant after the reaction is dark brown or black due to the formation of metal nanoparticles.

*NbCl*<sub>5</sub>, *MoCl*<sub>5</sub>, *AlCl*<sub>3</sub>·6 $H_2O$ . The supernatant after the reaction is blue due to the formation of the WCl<sub>6</sub> complex via etching of the WS<sub>2</sub> sheets.

Physical Characterization Methods. Transmission electron microscopy (TEM) images, selected-area electron diffraction patterns (SAED), and energy-dispersive X-ray spectroscopy (EDS) were acquired by using an FEI Tecnai T20 TEM equipped with a 200 kV LaB<sub>6</sub> filament and an Oxford Instruments X-MAX SDD EDS detector. High-angle annular dark field scanning transmission electron microscopy (HAADF-STEM) and EDS mapping were obtained on an FEI Talos F200X S/TEM with a 200 kV XFEG field-emission source and a super X-EDS system. Powder X-ray diffraction (XRD) measurements were acquired using a Panalytical Empyrean Powder Xray Diffractometer. The relative peak areas for the intercalated (001) peak and unintercalated (002) peak are utilized to determine the percentage of intercalation in each sample. A Panalytical Epsilon 4 Xray fluorescence spectrometer (XRF) was used for quantification of metal content. X-ray photoelectron spectroscopy (XPS) data were obtained with a Kratos AXIS Ultra Delay-Line Detector Imaging Xray Photoelectron Spectrometer. The survey XPS spectra are provided in Figure S12.

X-ray absorption spectroscopy (XAS) experiments were carried out at beamline 10-BM at the Advanced Photon Source (APS) in Argonne National Laboratory at the V K-edge (5465 eV), Cr K-edge

(5989 eV), Mn K-edge (6539 eV), Fe K-edge (7112 eV), Ga K-edge (10367 eV), and In K-edge (27940 eV) in transmission and fluorescence mode. All sample preparations were done under a nitrogen atmosphere. Samples were ground to a fine powder, diluted with carbon, and pressed to form a self-supported wafer. Spectra were recorded at room temperature. During each measurement, a metal foil or metal oxide film was scanned simultaneously through a third ion chamber for internal energy calibration. XAS data fitting was performed using the Demeter software package.<sup>39</sup> EXAFS coordination parameters were obtained by a least-squares fit in R-space of the  $k^2$ -weighed Fourier transform data from 3 to 8 Å<sup>-1</sup>. The reference metal foil or metal oxide was first fit to its known crystallographic structures in order to obtain an amplitude reduction factor  $(\tilde{S_0}^2)$  for the metal K-edge. EXAFS fitting of the first coordination shell was carried out between 1.0 and 3.0 Å in R-space. Fittings were performed by refining bond distances (R), coordination numbers (CN), energy shift  $(E_0)$ , and Debye–Waller factor  $(\sigma^2)$ .

Kelvin probe force microscopy (KPFM) measurements were conducted on an Asylum Cypher AFM instrument at room temperature. All samples were spun-coat onto a SiO2-passivated Si wafer and used immediately in the measurement. Platinum silicide coated probes (NANOSENSORS PtSi-FM) with approximately 30-120 nm spatial resolution and a calibrated spring constant of 2.8 N/m were utilized. The measurements were obtained in tapping mode with a lift height of 40 nm above the surface of the sample. In order to mitigate the influence of topographic artifacts across a 10  $\times$  10  $\mu m$ area due to surface roughness, contact potential difference (CPD) maps were generated from an area with a surface potential noise level less than 10 meV. A histogram of the measured CPD values was generated and then fit to two Gaussians to obtain the average CPD of the SiO<sub>2</sub> substrate and the sample. 40,41 Using the SiO<sub>2</sub> substrate as a reference with known work function of 5.00 eV, the work function of the three samples can be determined. 42,43

Raman spectroscopy and spatial mapping were carried out using a Thermo Scientific DXR3xi Raman Imaging Microscope with a 532 nm laser. In order to quantify the area percentage of the 1T' and 2H phase in a given sample, three 50  $\times$  50  $\mu m$  areas were mapped for each sample with a spatial resolution of 1  $\mu m$ . Each image was normalized by the peak intensity at 130 cm $^{-1}$  (for the 1T' phase) or 414 cm $^{-1}$  (for the 2H phase), and the number of pixels containing the specified peak was quantified.

**Electronic Characterization Methods.** Electronic measurements were conducted on circular pellets in a four-point van der Pauw configuration. Hahrs Typically, 50 mg of sample powder was loaded into a pellet press die with 6 mm diameter and pressed under 3000 pounds (48 GPa) of pressure. The resulting pellets had thicknesses of  $170 \pm 50 \, \mu$ m. Gold contacts were then evaporated onto the pellet in a four-point van der Pauw geometry. All of the gold contacts were kept smaller than  $1 \times 1 \, \text{mm}$  to keep the measurement error low ( $\leq 1\%$ ).

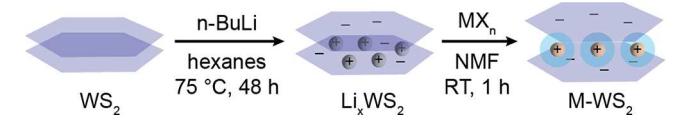
Temperature-dependent resistance was measured using a Quantum Design DynaCool Physical Property Measurement System (PPMS) from 60 to 300 K. The average sheet resistance (R) for the pellet is calculated from multiple individual measurements. Sample resistivity ( $\rho$ ) and conductivity ( $\sigma$ ) were calculated from the pellet thickness and measured average sheet resistance. Carrier transport activation energies ( $E_{\rm a}$ ) were obtained by fitting the temperature-dependent conductivity measurements to the Arrhenius equation (eq 1) between 300 and 100 K, where  $\sigma$  is the conductivity (S/cm), A is a constant,  $E_{\rm a}$  is the activation energy (eV), k is the Boltzmann constant (8.617 ×  $10^{-5}$  eV/K), and T is the temperature (K).

$$\sigma = Ae^{-E_a/kT} \tag{1}$$

#### RESULTS AND DISCUSSION

The overall synthetic process for generating metal-intercalated WS<sub>2</sub> samples is illustrated in Scheme 1. We began by screening 17 transition-metal halide precursors in our previously reported synthetic method, varying both the metal atom

Scheme 1. Two-Step Synthetic Method for the Intercalation of Transition-Metal and Post-Transition-Metal Cations into WS<sub>2</sub>



identity and oxidation state (Figure 1a,b). <sup>35</sup> Briefly, bulk 2H-WS<sub>2</sub> is stirred with 0.5 M n-BuLi at elevated temperature to simultaneously drive electron transfer to WS<sub>2</sub>, Li<sup>+</sup> intercalation, and phase transformation from the semiconducting 2H phase to the semimetallic 1T' phase as evidenced by the shift in powder XRD (00n) peak and appearance of superlattice spots in the SAED pattern (Figures 1c, S1). These observations are in accord with extensive literature reports on the lithation of WS<sub>2</sub> using a variety of chemical reductants. <sup>29,30,38</sup> The resulting 1T'-Li<sub>x</sub>WS<sub>2</sub> powder is stirred with 2 equiv of the TM precursor in N-methylformamide (NMF) for 1 h under a N<sub>2</sub> atmosphere. For clarity, each TM-intercalated WS<sub>2</sub> sample will be labeled by its precursor, because the product may contain multiple redox states and morphologies.

Powder XRD (Figure 1c) and TEM with SAED (Figure 1d) were used as initial screening tools to determine whether intercalation occurred successfully and if any other morphologies were present in the system. Representative examples of different product heterostructures are shown in Figure 1, and all other sample data are provided in Figures S2–S7. In the powder XRD, intercalated structures show a characteristic shift in the (00n) diffraction peak to lower  $2\theta$  values, representing an expansion of the interlayer spacing (d). The (00n) peaks for bulk WS<sub>2</sub> ( $2\theta = 14.3^{\circ}$ , d = 6.2 Å) and Li<sub>x</sub>WS<sub>2</sub> ( $2\theta = 13.9^{\circ}$ , d = 6.4 Å) are shown for comparison. The relative area of the intercalated and unintercalated (00n) peaks is used to quantify the percentage of intercalation in each sample.

Based on this initial screening, we observed three distinct heterostructures: TM-intercalated WS<sub>2</sub>, secondary nucleated

nanoparticles supported on or around WS2, and etching of the WS<sub>2</sub>. The two factors that appear to exert the greatest influence on product morphology are the precursor charge density, calculated by dividing the cationic charge by the ionic radius, and the metal ion standard reduction potential  $(E_{red})$  (Figure 1b).46-48 We find that metal precursors with higher charge density, i.e., more positive charge and smaller size, selectively intercalate into the layered structure because of the strong electrostatic interaction between the cationic intercalant and anionic WS<sub>2</sub> sheets. Specifically, metal ion intercalation occurs preferentially over secondary nucleation when the precursor charge density is between +3 and +5. CrCl<sub>3</sub>-WS<sub>2</sub> is one such example that shows exclusively the shifted (00n) peak at  $6.2^{\circ}$ corresponding to an expanded interlayer spacing, no evidence of secondary nucleation in the TEM image, and retention of 1T' single-crystallinity in the SAED. In contrast, precursors with charge density <+3 tend to secondary nucleate due to their weaker electrostatic interaction with the anionic WS2, resulting in metal oxide aggregates for less reducible ions and metallic nanoparticles for more reducible ions. ZnCl<sub>2</sub>-WS<sub>2</sub> and CuCl-WS2 represent the oxidized and reduced regimes, respectively, with both clearly showing small nanoparticles along the edges of the WS2 microsheets. In both cases, the intercalated (00n) peak is observed in XRD, but intercalation is incomplete, as the bulk WS2 peak at 14.3° remains. If the precursor charge density exceeds +5, significant etching and decomposition of the WS2 sheets is observed due to the high Lewis acidity of the metal ion. 49 As a representative example, AlCl<sub>3</sub>-WS<sub>2</sub> shows no intercalation peak in the powder XRD, pronounced degradation of the micrometer-sized WS<sub>2</sub> sheets based on the TEM image, and loss of crystallinity in the SAED pattern (Figure 1c,d). Notably, Li<sup>+</sup> deintercalation is observed during this process, with the lithiated XRD peak shifting back to the unintercalated WS<sub>2</sub> peak position. A control experiment in which Li<sub>x</sub>WS<sub>2</sub> is stirred in NMF alone without any added cations shows that the presence of solvent is sufficient to drive Li<sup>+</sup> deintercalation (Figure S18).

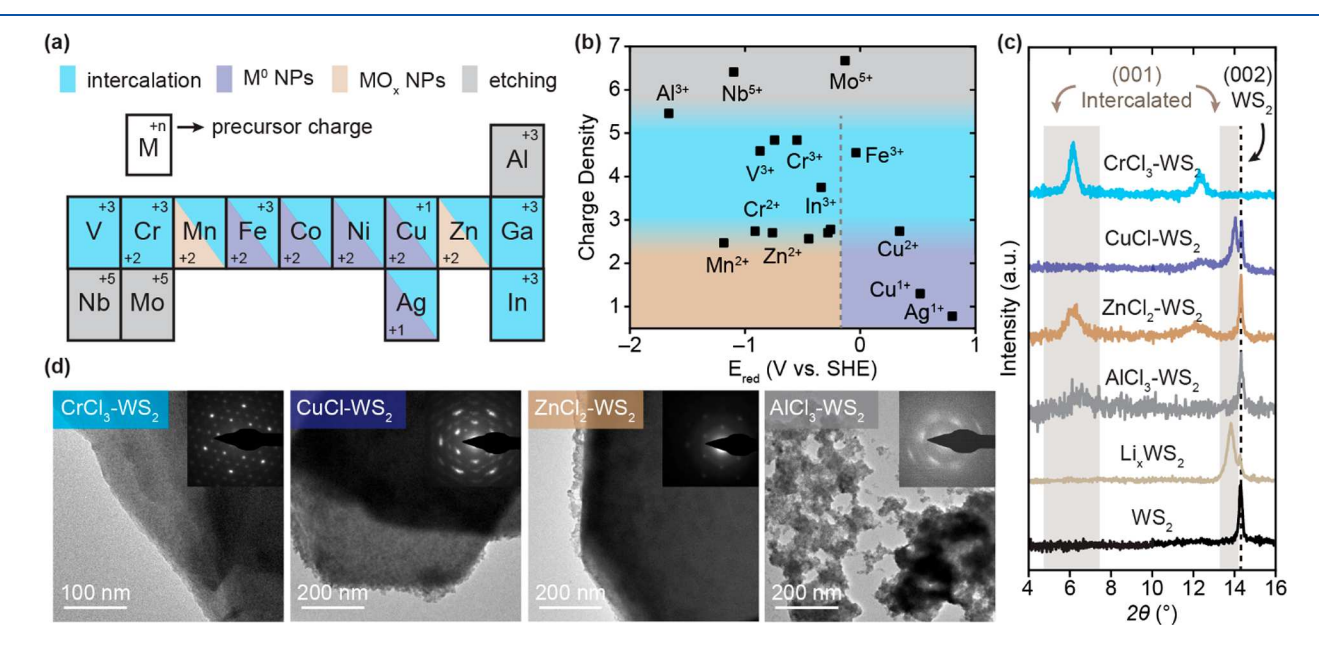


Figure 1. (a) Summary of all transition-metal ions studied in the intercalation reaction and the resulting TM-WS<sub>2</sub> morphologies. (b) Plot of charge density vs standard reduction potential for all TM precursors with shaded regions representing the dominant morphology. (c) Powder XRD patterns, (d) TEM images, and SAED patterns (inset) of representative TM-WS<sub>2</sub> samples with different heterostructures.

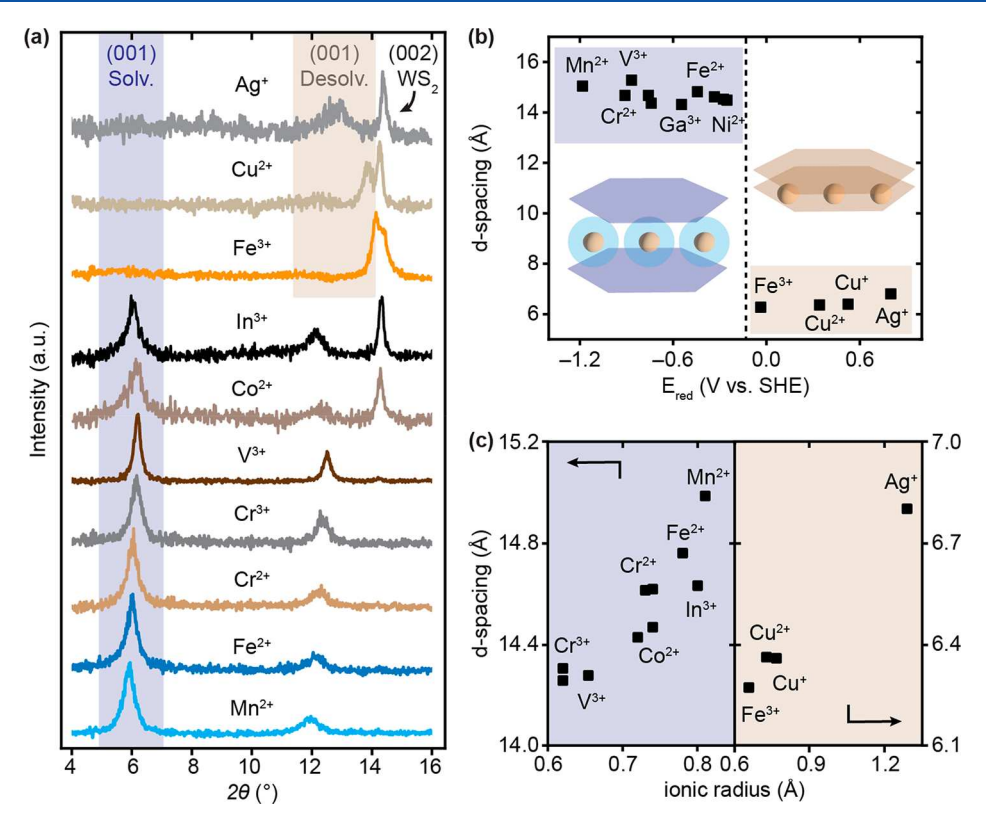


Figure 2. (a) Powder XRD patterns of selected TM-WS<sub>2</sub> samples with shaded regions highlighting the (001) peaks for solvated and desolvated intercalants. (b,c) TM-WS<sub>2</sub> interlayer spacing plotted vs the (b) standard reduction potential and (c) ionic radius of the TM precursor.

Comparing the powder XRD patterns of the 17 TM-WS<sub>2</sub> samples, we observe that all transition-metal precursors intercalate to some degree except for those that etch the WS<sub>2</sub> (Figures 2a, S2-S7, Table S1). Two distinct d-spacing regimes are observed in the TM-intercalated WS<sub>2</sub> structures, which depend upon the standard reduction potential of the metal precursor (Figure 2b). Less reducible transition-metal halides ( $E_{\text{red}} < -0.1 \text{ V vs SHE}$ ) generate very large *d*-spacings upon intercalation (14-16 Å), which has been shown previously to stem from the incorporation of large, solvated cation complexes.<sup>50</sup> Most samples in this regime are fully intercalated, where the XRD peak at 14.3° corresponding to pristine bulk WS<sub>2</sub> is no longer observed. Only a few samples that display heterogeneous product morphologies (Zn<sup>2+</sup>, Co<sup>2+</sup>, Ni<sup>2+</sup>, and In<sup>3+</sup>) retain the unintercalated WS<sub>2</sub> feature. In contrast, the more reducible transition-metal halides ( $E_{red}$  > -0.1 V vs SHE) exhibit d-spacings of 6-7 Å, similar to that of intercalated Li<sup>+</sup> and representing only a small expansion relative to bulk WS<sub>2</sub>. This d-spacing regime is similar to materials synthesized through zerovalent intercalation, 21,51-54 which suggests that more reducible metal ions intercalate as reduced and desolvated species. All of these samples show some quantity of unintercalated WS2, which is most significant when secondary nucleation dominates, as in Cu and Ag.

Further analysis in each regime shows a correlation between the observed *d*-spacing and the ionic radius of the precursor metal species. In both solvated and desolvated regimes, intercalated ions follow the expected trend where larger ionic radii lead to larger *d*-spacing upon intercalation (Figure 2c). Because the size of hydrated complexes follows that of the bare ions as long as they exhibit similar coordination geometries, <sup>46</sup> these data suggest that the metal oxidation state and pseudo-octahedral coordination environment of the solvated complex

remain relatively constant after intercalation. In the desolvated intercalant regime, we anticipate that all metal ions are reduced to some degree, so the trend in size holds.

The quantity of transition metal incorporated into the sample, expressed as an atomic ratio of TM to W, is also highly dependent on the product heterostructure. Etched samples (Al, Nb, Mo) show negligible amounts of the TM based on EDS and XRF elemental analysis (Figure S8, Table S1). In the secondary nucleated region, the atomic ratios of the more reducible TMs (Cu, Ag, Fe) tend to be quite high (>0.5) due to the formation of metallic nanoparticles supported on WS<sub>2</sub>. Secondary nucleation of metal oxide nanoparticles through hydrolysis (Zn, Mn) results in lower atomic ratios (0.07–0.17) of incorporated transition metals, in part because the oxidized species are more easily washed away at the end of the synthesis. Metal ions that undergo only intercalation show a fairly broad range of transition-metal incorporation (0.18 to 0.63) even though the majority of samples show only the intercalated (00n) peak in the XRD (Table S1).

We conducted additional characterization on all of the intercalated TM-WS<sub>2</sub> samples that do not contain secondary nucleated structures. Within this family of samples, further distinctions in morphology can be observed. We characterize examples of TM-WS<sub>2</sub> materials that show uniform intercalation of solvated cations (Figure 3a) and desolvated cations (Figure 3b) as well as examples with surface enrichment of the TM (Figure 3c).

 $CrCl_3$ – $WS_2$  (Figure 3a) is an example of a sample with relatively uniform intercalation of solvated cations, where the bulk  $WS_2$  (00n) peak is completely suppressed and the intercalated d-spacing is observed at 14.3 Å (Figure 2a). STEM-EDS mapping reveals a uniform Cr:W ratio of 0.25 across the lateral area of the nanosheet. XPS, a surface sensitive

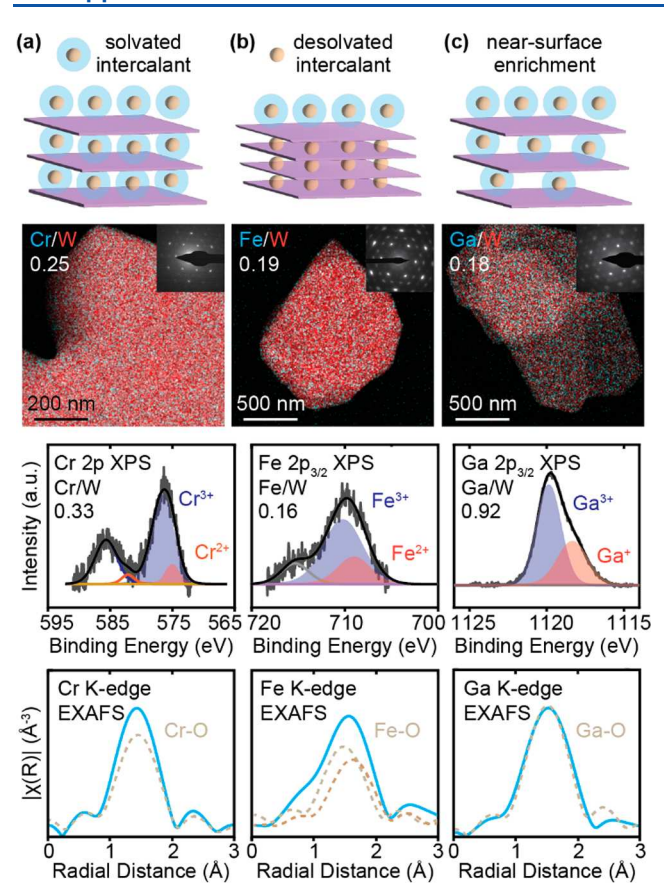


**Figure 3.** Characterization of  $TM-WS_2$  samples representing the (a) uniform distribution of solvated intercalants, (b) uniform distribution of desolvated intercalants, and (c) surface enrichment of solvated intercalants. For each sample, EDS maps, high-resolution XPS of the TM 2p region, and EXAFS at the TM K-edge are provided.

technique, provides an estimate of the near-surface atomic ratio of the intercalant. In this case, the surface Cr:W ratio is 0.33, which is fairly similar to the bulk atomic ratio and indicative of a vertically homogeneous distribution of TM intercalants. XPS of the Cr 2p region also shows that the majority of ions remain in the +3 oxidation state, with <10% reduced to the Cr<sup>2+</sup> state. X-ray absorption spectroscopy corroborates the solvated structure of Cr3+ ions with no secondary nucleation. X-ray absorption near-edge spectroscopy (XANES) shows a Cr K-edge energy of 6001 eV, consistent with that of the Cr3+ oxidation state. In the X-ray absorption fine structure (EXAFS), CrCl<sub>3</sub>-WS<sub>2</sub> shows only a first coordination sphere scattering peak at a short radial distance, as expected for isolated metal complexes with oxygen-based ligands. The Cr EXAFS fits well to a single Cr-O scattering path with a radial distance of 1.97 Å (Table S2), revealing that the Cr intercalants remain primarily solvent-coordinated and have a relatively weak interaction with the host WS<sub>2</sub> sheets. VCl<sub>3</sub>-WS<sub>2</sub>, which we studied in detail in our previous work, exhibits a structure similar to that of CrCl<sub>3</sub>-WS<sub>2</sub> with uniformly solvated cations.

Samples with uniformly desolvated TM intercalants, exemplified by  $FeCl_3$ –WS<sub>2</sub>, show structural properties very similar to those described above but with a much smaller (00*n*) *d*-spacing (Figures 3b, 2a). EDS mapping shows a laterally homogeneous distribution of Fe in WS<sub>2</sub> at an atomic ratio of 0.19, which is similar to the surface atomic ratio of 0.16. Fe 2p

XPS shows predominantly Fe<sup>3+</sup> ions, and the Fe K-edge XANES energy of 7123 eV matches fairly closely the expected value for Fe<sup>3+</sup> (Figure S13). EXAFS shows only a first coordination sphere scattering peak, indicating that Fe atoms remain isolated in the interlayer galleries in this sample.

GaCl<sub>3</sub>-WS<sub>2</sub> (Figure 3c) shows near-surface enrichment of Ga ions on the WS<sub>2</sub> microparticles as well as intercalation in the bulk. The lateral distribution of Ga in the EDS map is quite uniform at 0.18 relative to W. The XPS, however, shows a surface Ga:W atomic ratio of 0.97, >5 times higher than the bulk ratio, indicating a strong surface enrichment of Ga species. XPS and Ga K-edge XANES (Figure S13) show partial reduction of Ga<sup>3+</sup> to Ga<sup>+</sup>, and EXAFS reveals that Ga centers are fully oxygen-coordinated, consistent with the intercalation of the solvated complexes. InCl<sub>3</sub>-WS<sub>2</sub> and CrCl<sub>2</sub>-WS<sub>2</sub> also show varying degrees of metal surface enrichment (Figure S9). We postulate that surface enrichment occurs when ion diffusion within the interlayer galleries of WS2 is relatively slow. Previous work in the literature on alkali ion intercalation in layered materials has shown that strong electrostatic interactions between high charge density cations and anionic hosts frequently result in nonuniform intercalation due to a high kinetic barrier toward cation diffusion from the edges to the center of the sheet. 55-61 This dynamic is likely also at play in our near-surface-enriched TM-WS2 samples.

We also characterized two TM-WS<sub>2</sub> samples with secondary nucleated species. MnCl2-WS2 contains both intercalated Mn<sup>2+</sup> complexes (Figure S6) and metal oxide nanoparticles (Figures S10, S11). The Mn K-edge EXAFS (Figure S10) has two strong scattering peaks corresponding to the first coordination sphere Mn-O scattering path and the second coordination sphere Mn-O-Mn scattering path, which are diagnostic of the presence of MnO<sub>x</sub> aggregates. FeCl<sub>2</sub>-WS<sub>2</sub> comprises a mixture of intercalated solvated complexes (Figure S4) and secondary nucleated Fe<sup>0</sup> species forming a shell around the edges of the WS<sub>2</sub> microsheet (Figures S10, S11). The partial reduction of Fe<sup>2+</sup> to Fe<sup>0</sup> is evident in the XANES K-edge energy, which shifts from 7120 to 7118 eV after intercalation (Figure S13).62 The Fe K-edge EXAFS shows both the Fe-O scattering path expected for the solvated Fe<sup>2+</sup> complex and an Fe-Fe scattering path at 2.57 Å consistent with Fe metal (Tables S2, S3).

Based on all of the transition-metal precursors studied herein, we postulate that the observed differences in product morphology stem from differences in the relative rates of metal ion reduction, cation diffusion, and secondary nucleation for each metal ion (Figure 4). In the case of Fe<sup>3+</sup>, as well as the other highly reducible metal ions Cu<sup>1+/2+</sup>, and Ag<sup>+</sup>, the metal ion reduces rapidly upon contact with the LixWS2 nanosheets and undergoes zerovalent intercalation into WS2 (bottom pathway). Subsequent charge transfer between the M<sup>0</sup> atom and the conduction band of the 2D material results in partially oxidized, desolvated intercalants. This type of mechanism has been shown in NbS2 and TaS2 with a wide variety of transitionmetal atoms. 5,12,13,22 Zerovalent intercalation competes with secondary nucleation in this scenario, and the relative rates of those two processes dictate the distribution of intercalated ions and supported metallic nanoparticles. For ions at the boundary of both charge density and reducibility relative to the LixWS2 sheets, namely Fe<sup>2+</sup>, Co<sup>2+</sup>, and Ni<sup>2+</sup>, reduction of the cations to M<sup>0</sup> atoms is slower than both intercalation and secondary nucleation, leading to a mixture of solvated M<sup>2+</sup> intercalants and a  $MO_x$  shell surrounding the  $WS_2$  (top pathway).

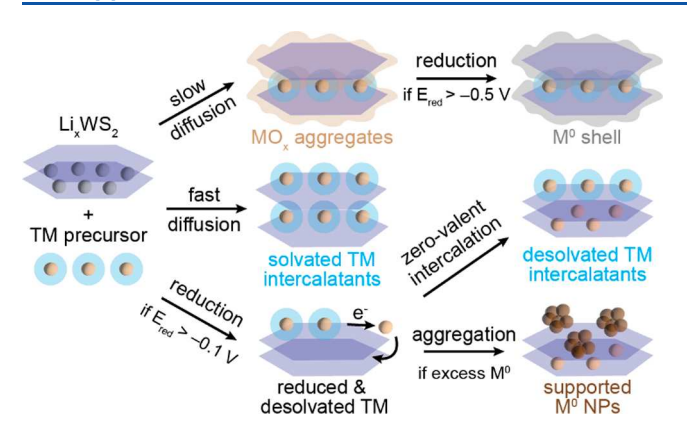


**Figure 4.** Summary of reaction pathways observed in the reaction of TM precursors with Li<sub>x</sub>WS<sub>2</sub>.

Subsequent reduction of the  $MO_x$  shell by  $Li_xWS_2$  leads to the formation of a distinct ring of  $M^0$  in these three cases that is not observed when the ion is reduced first prior to secondary nucleation, as is the case in the Ag sample (Figure S11). Finally, nonreducible ions with high charge density selectively interact with the anionic  $WS_2$  layers, undergoing only intercalation as the solvated complex (middle pathway), though nonuniformity in the surface/bulk distribution is observed for slower diffusing cations. Together, our study of TM intercalation into  $Li_xWS_2$  reveals a complex interplay among intercalation, diffusion, secondary nucleation, and reduction. Understanding and controlling these relative rates are critical to achieving uniform intercalation.

In addition to the diverse structures observed at the transition-metal center, the crystal structure of WS<sub>2</sub> is also strongly influenced by TM intercalation. Raman spectroscopy provides the clearest distinction between the trigonal prismatic 2H phase ( $E_{2g}$  and  $A_{1g}$  peaks at 350 and 414 cm<sup>-1</sup>) observed in bulk WS<sub>2</sub> and the distorted octahedral 1T' phase ( $J_1$  and  $J_2$  peaks at 130 and 250 cm<sup>-1</sup>) formed upon lithiation and TM

intercalation (Figure 5a). Interestingly, we find that the relative intensities of the  $J_1$  and  $J_2$  peaks vary significantly across the TM-WS<sub>2</sub> samples. The  $J_2$  vibrational mode contains significant out-of-plane motion <sup>33,63,64</sup> and is only observed in the samples with relatively uniform intercalant distribution through the thickness of the WS<sub>2</sub> microsheet (FeCl<sub>3</sub>–, VCl<sub>3</sub>–, CrCl<sub>3</sub>– WS<sub>2</sub>). Heterogeneity in the intercalant distribution and interlayer coupling likely leads to broadening of the  $J_2$  feature and eventual disappearance of the peak in the most disordered samples.

To quantify the area percentage of 1T' vs 2H phase, Raman mapping data are collected and color-coded based on the presence of the J<sub>1</sub> (1T') and A<sub>1g</sub> (2H) peaks. Shown in Figure 5b, the green pixels contain only 1T' peaks, the red pixels contain only 2H, and the yellow pixels contain a mixture of the two phases. Previously, we showed that uniform intercalation of V ions stabilized the 1T' phase of WS2 during the solutionphase cation-exchange reaction due to their interaction with the basal planes of WS<sub>2</sub>.<sup>35</sup> Stirring the Li<sub>x</sub>WS<sub>2</sub> material with solvent alone led to a loss of Li<sup>+</sup> and reversion to the 2H phase. This trend holds across the TMs studied herein. FeCl<sub>3</sub>-WS<sub>2</sub>, CrCl<sub>3</sub>-WS<sub>2</sub>, and GaCl<sub>3</sub>-WS<sub>2</sub> represent samples with high, medium, and low area percentages of the 1T' phase (Figure 5b, Table S1). The quantity of the 1T' phase retained after intercalation is directly correlated to the uniformity of the TM intercalant through the thickness of the WS2 microsheet. A simple metric for intercalant uniformity is the ratio of the bulk to surface TM concentration as measured by EDS and XPS, respectively. TM-WS<sub>2</sub> samples with bulk/surface ratios near or greater than 1 (FeCl<sub>3</sub>-, VCl<sub>3</sub>-WS<sub>2</sub>) are highly uniform in distribution and show >80% 1T' retention based on Raman mapping (Figure 5c). As the sample becomes more surfaceenriched and less uniformly distributed (bulk/surface ratio <0.5), the percentage of 1T' phase drops correspondingly (Figure S15). Since the W 4f XPS binding energy is also diagnostic of the WS2 phase, we can quantify the near-surface

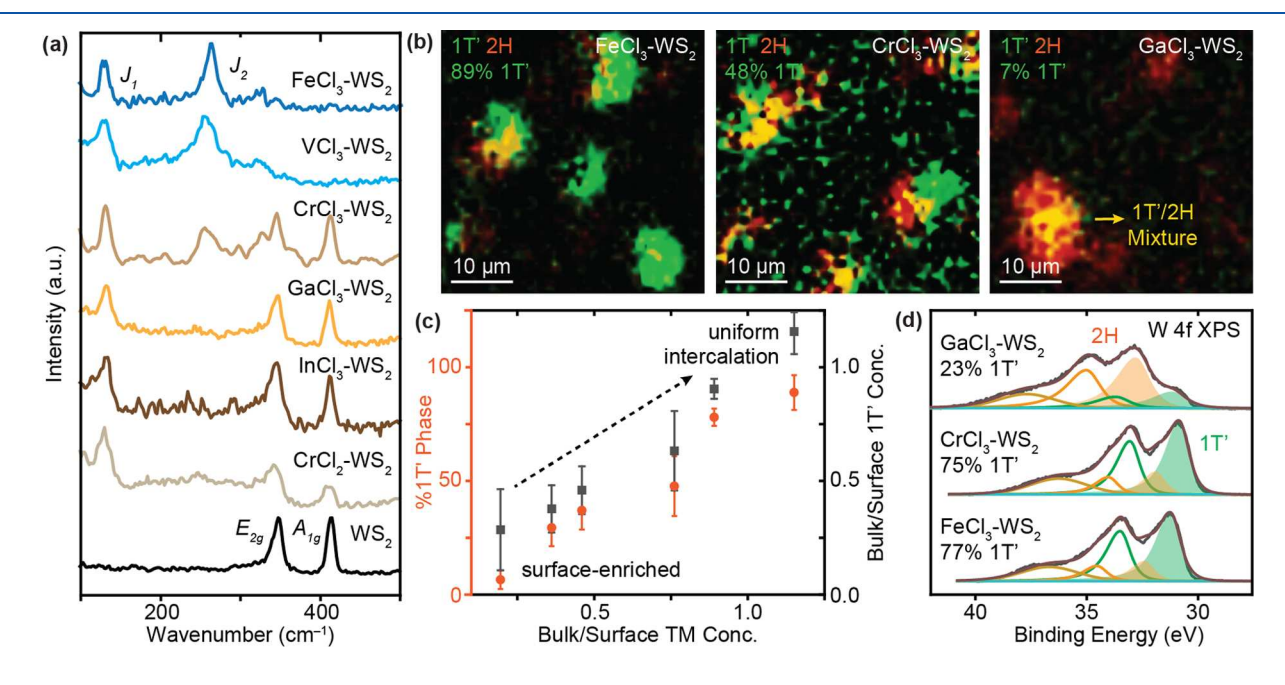
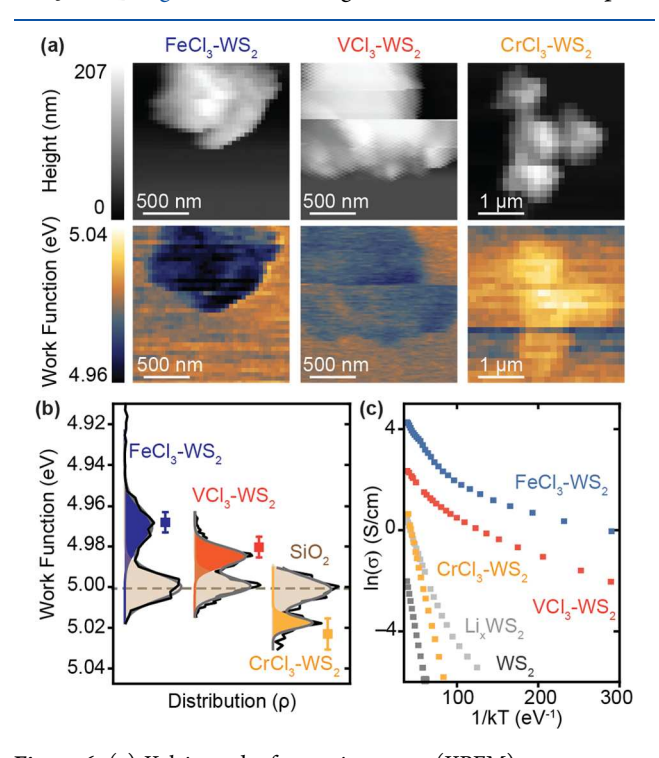


Figure 5. (a) Raman spectra of intercalated TM-WS<sub>2</sub> samples. (b) Raman maps of FeCl<sub>3</sub>–, CrCl<sub>3</sub>–, and GaCl<sub>3</sub>–WS<sub>2</sub>. (c) Correlating the %1T′ phase and bulk to surface 1T′ ratio with the bulk to surface ratio of the TM concentration. (d) W 4f XPS spectra of FeCl<sub>3</sub>–, CrCl<sub>3</sub>–, and GaCl<sub>3</sub>–WS<sub>2</sub>.

1T' concentration by XPS (Figures 5d, S16). As anticipated, the bulk/surface ratios of the TM and 1T' concentrations correlate closely with one another, supporting the fact that the presence of interlayer TM ions in the bulk stabilizes the 1T' phase during the solution-phase reaction (Figure 5c).

Finally, we studied the electronic properties of the uniformly intercalated TM-WS<sub>2</sub> samples: FeCl<sub>3</sub>–WS<sub>2</sub>, CrCl<sub>3</sub>–WS<sub>2</sub>, and VCl<sub>3</sub>–WS<sub>2</sub>. Figure 6a shows height and work function maps of



**Figure 6.** (a) Kelvin probe force microscopy (KPFM) measurements showing the height and work function maps of FeCl<sub>3</sub>–WS<sub>2</sub>, CrCl<sub>3</sub>–WS<sub>2</sub>, and VCl<sub>3</sub>–WS<sub>2</sub>. (b) Histograms of the measured work function values extracted from the spatial map. (c) Temperature-dependent conductivity plotted as  $\ln \sigma$  vs 1/kT.

the three samples measured by Kelvin probe force microscopy (KPFM). FeCl<sub>3</sub>-WS<sub>2</sub> has the smallest average work function of 4.97 eV, while CrCl<sub>3</sub>-WS<sub>2</sub> has the highest work function of 5.02 eV, all of which are lower than the precursor Li<sub>x</sub>WS<sub>2</sub> at 5.06 eV (Figure 6b).<sup>35</sup> The 90 meV drop in work function between FeCl<sub>3</sub>-WS<sub>2</sub> and Li<sub>x</sub>WS<sub>2</sub> reflects a comparable upward shift in the Fermi level, which we hypothesize arises from hybridization of TM intercalant d-orbitals with the bands of WS<sub>2</sub>. The increase in Fermi energy leads to FeCl<sub>3</sub>–WS<sub>2</sub> having the highest room-temperature conductivity (110 S/cm) and the lowest carrier activation energy (18 meV) among the bulk and intercalated WS<sub>2</sub> samples studied herein (Figure 6c). In contrast, CrCl<sub>3</sub>-WS<sub>2</sub> shows a conductivity of 1.9 S/cm and activation energy of 143 meV, which is fairly similar to the electronic behavior of Li<sub>x</sub>WS<sub>2</sub>. Our previous measurements of bulk WS<sub>2</sub>, Li<sub>x</sub>WS<sub>2</sub>, and VCl<sub>3</sub>-WS<sub>2</sub> are included for comparison in Figure 6c. VCl<sub>3</sub>-WS<sub>2</sub> falls between the Fe and Cr samples with room-temperature conductivity of 12 S/cm and an  $E_a$  of 20 meV. The electronic characterization supports the fact that stronger binding of the TM intercalants to the WS2 sheets results in greater modulation of their electronic properties.

As controls, we also obtained electronic measurements for FeCl<sub>2</sub>–WS<sub>2</sub> and CrCl<sub>2</sub>–WS<sub>2</sub> that contained a surface shell of Fe<sup>0</sup> or surface enrichment of Cr complexes (Figure S17). The

FeCl<sub>2</sub>–WS<sub>2</sub> sample, in particular, shows much lower room-temperature conductivity (3.2 S/cm) and higher carrier activation energy (65 meV) than FeCl<sub>3</sub>–WS<sub>2</sub>, confirming that the presence of metallic impurities at the grain boundaries is not responsible for the improvement of electronic properties. CrCl<sub>2</sub>–WS<sub>2</sub> also shows lower conductivity (0.58 S/cm) relative to that of the more uniformly intercalated CrCl<sub>3</sub>–WS<sub>2</sub> (Figure S17). Of the TM-intercalated WS<sub>2</sub> materials that we studied, FeCl<sub>3</sub>–WS<sub>2</sub> is the only one that shows uniform intercalation of desolvated cations, which leads to the largest shift in Fermi level and greatest improvement in electronic transport properties compared to the weaker-bound solvated Cr and V cations.

To better understand the electronic properties of the FeCl<sub>3</sub>-WS<sub>2</sub> sample, we performed density functional theory (DFT) calculations on 1T'-WS2 bulk materials with and without intercalated Fe atoms. Computational details are provided in the Supporting Information. Both tetrahedral  $(T_d)$ and octahedral (O<sub>h</sub>) binding geometries were considered for intercalated Fe atoms at a 0.25 atomic ratio with respect to W (Figure S21). Oh coordination for Fe atoms in the interlayer space is more stable than  $T_{\rm d}$  by 0.25 eV and results in a narrower interlayer spacing of 6.22 Å, which corresponds well with the experimental d-spacing in FeCl<sub>3</sub>-WS<sub>2</sub> (Table S1). Based on the greater stability and close match to experimental XRD data, we postulate that intercalated Fe atoms in our system are primarily Oh in geometry with some conformational heterogeneity and disorder. The calculated band structure and projected density of states are shown for unintercalated 1T'-WS<sub>2</sub> and the  $O_h$  Fe<sub>0.25</sub>WS<sub>2</sub> in Figure 7 and the  $T_d$  Fe<sub>0.25</sub>WS<sub>2</sub> in Figure S22. In both binding geometries, intercalated Fe atoms serve primarily as electron donors to WS2, as seen from the contribution of Fe d-orbitals to states at and below the Fermi level. The Fe contribution leads to an overall upward shift in the Fermi level of the system. To more quantitatively obtain the Fermi energy of these systems, a model of the 1T'-WS<sub>2</sub> surface was constructed, and the energy required to remove an electron at the surface to the vacuum level was explicitly calculated (Figures S23-S25). These data reveal an upward shift in Fermi energy of 70 meV for  $O_h$  and 50 meV for  $T_d$ Fe<sub>0.25</sub>WS<sub>2</sub> compared with 1T'-WS<sub>2</sub>, consistent with both the band structure calculation and the experimental KPFM measurements.

## CONCLUSION

In conclusion, we have demonstrated that the charge density and reduction potential are key factors influencing the intercalation of TM complexes in WS2 through cation diffusion. By limiting the charge density of TM complexes to a range between 3 and 5, TMs can be selectively intercalated into WS<sub>2</sub> with minimal secondary nucleation and degradation. Three distinct morphologies of TM-intercalated WS<sub>2</sub> are characterized, comprising different levels of intercalation, 1T'phase retention, and surface segregation. FeCl<sub>3</sub>-WS<sub>2</sub> shows the strongest interaction between Fe<sup>2/3+</sup> intercalants and the WS<sub>2</sub> sheets, exhibiting the narrowest interlayer spacing and the highest degree of 1T' phase retention. As a result, the conductivity of the sample increases by 3 orders of magnitude relative to pristine WS2. This systematic study of a wide array of TM-intercalated WS<sub>2</sub> structures not only enriches the compositional diversity of layered TMDs but also provides general design principles for achieving selective intercalation in

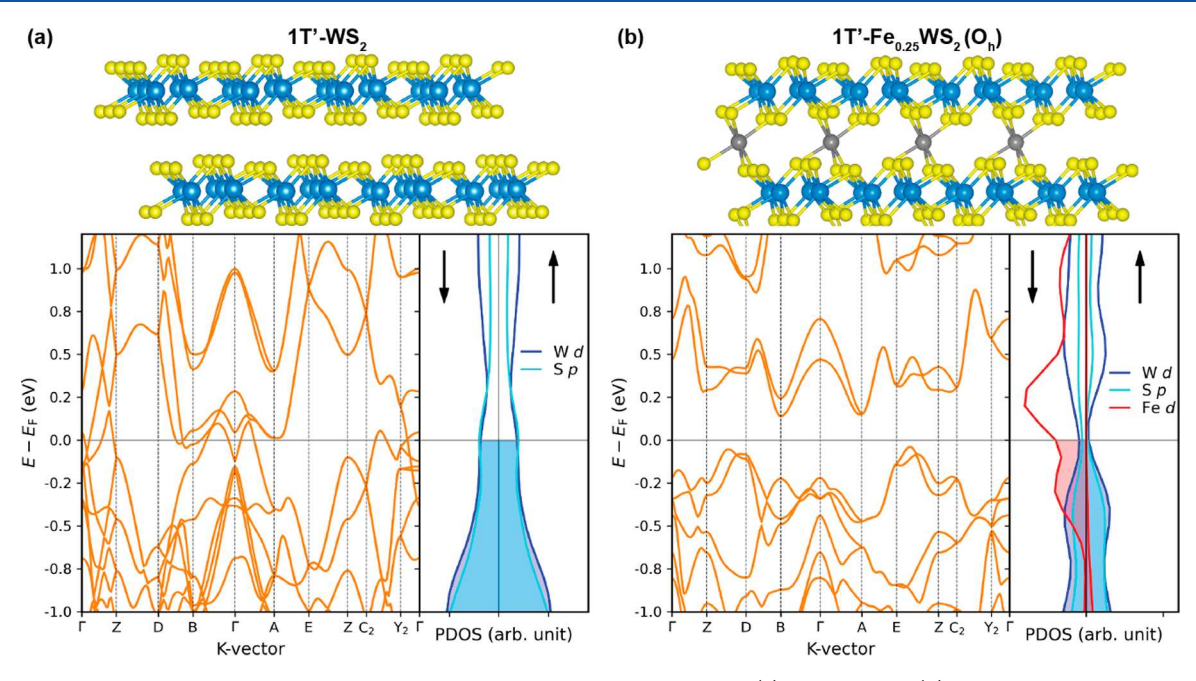


Figure 7. Structural models, calculated band structure, and projected density of states for (a) 1T'-WS<sub>2</sub> and (b) 1T'-Fe<sub>0.25</sub>WS<sub>2</sub> with Fe atoms in an octahedral (O<sub>b</sub>) coordination environment.

layered TMDs for eventual application in flexible, nanoscale electronics.

#### ASSOCIATED CONTENT

# **Solution** Supporting Information

The Supporting Information is available free of charge at https://pubs.acs.org/doi/10.1021/acsanm.3c03028.

Materials, computational methods, supplementary figures, and supplementary tables including additional physical characterization data and EXAFS fitting parameters (PDF)

#### AUTHOR INFORMATION

### **Corresponding Author**

Christina W. Li — Department of Chemistry, Purdue University, West Lafayette, Indiana 47907, United States; orcid.org/0000-0002-3538-9955; Email: christinawli@purdue.edu

#### **Authors**

Kuixin Zhu — Department of Chemistry, Purdue University, West Lafayette, Indiana 47907, United States

Yiyin Tao — Department of Chemistry, Purdue University, West Lafayette, Indiana 47907, United States

Sagarmoy Mandal — Department of Chemistry, Purdue University, West Lafayette, Indiana 47907, United States

Ming Chen — Department of Chemistry, Purdue University, West Lafayette, Indiana 47907, United States; ⊚ orcid.org/0000-0001-6205-7107

Complete contact information is available at: https://pubs.acs.org/10.1021/acsanm.3c03028

#### Notes

The authors declare no competing financial interest.

#### ACKNOWLEDGMENTS

This work was supported by the National Science Foundation (CHE-2106450). S.M. and M.C. gratefully acknowledge support from the National Science Foundation (EAR-2246687). We acknowledge Zhifan Ke and Professor Jianguo Mei for their help in depositing Au contacts for electronic measurements. We acknowledge Dr. Yujia Ding, Dr. Carlo Segre, and Dr. Joshua Wright for their assistance with XAS experiments. XAS data was collected at beamline 10-BM at the Advanced Photon Source (APS), Argonne National Laboratory. Use of the APS is supported by the U.S. Department of Energy, Office of Science, Office of Basic Energy Sciences, under Contract DE-AC02-06CH11357. MRCAT operations are supported by the Department of Energy and the MRCAT member institutions. XPS data was obtained at the Surface Analysis Facility of the Birck Nanotechnology Center, Purdue University. Computational resources were provided by the National Energy Research Scientific Computing Center (NERSC), a U.S. Department of Energy Office of Science User Facility, operated under Contract No. DE-AC02-05CH11231.

#### REFERENCES

- (1) Moore must go on. Nat. Nanotechnol., 2023, 18, 421-421.
- (2) Radisavljevic, B.; Radenovic, A.; Brivio, J.; Giacometti, V.; Kis, A. Single-layer MoS<sub>2</sub> transistors. *Nat. Nanotechnol.* **2011**, *6*, 147–150.
- (3) Wu, F.; Tian, H.; Shen, Y.; Hou, Z.; Ren, J.; Gou, G. Y.; Sun, Y. B.; Yang, Y.; Ren, T. L. Vertical MoS2 transistors with sub-1-nm gate lengths. *Nature* **2022**, *603*, 259–264.
- (4) Yang, X. D.; Li, J.; Song, R.; Zhao, B.; Tang, J. M.; Kong, L. A.; Huang, H.; Zhang, Z. W.; Liao, L.; Liu, Y.; Duan, X. F.; Duan, X. D. Highly reproducible van der Waals integration of two-dimensional electronics on the wafer scale. *Nat. Nanotechnol.* **2023**, *18*, 471–478.
- (5) Liu, X. C.; Zhao, S.; Sun, X.; Deng, L.; Zou, X.; Hu, Y.; Wang, Y. X.; Chu, C. W.; Li, J.; Wu, J.; Ke, F. S.; Ajayan, P. M. Spontaneous self-intercalation of copper atoms into transition metal dichalcogenides. *Sci. Adv.* **2020**, *6*, No. aay4092.
- (6) Gong, Y.; Yuan, H.; Wu, C. L.; Tang, P.; Yang, S. Z.; Yang, A.; Li, G.; Liu, B.; Van De Groep, J.; Brongersma, M. L.; Chisholm, M. F.;

- Zhang, S. C.; Zhou, W.; Cui, Y. Spatially controlled doping of two-dimensional SnS<sub>2</sub> through intercalation for electronics. *Nat. Nanotechnol.* **2018**, *13*, 294–299.
- (7) Zhang, J.; Sun, J.; Li, Y.; Shi, F.; Cui, Y. Electrochemical Control of Copper Intercalation into Nanoscale Bi<sub>2</sub>Se<sub>3</sub>. *Nano Lett.* **2017**, *17*, 1741–1747.
- (8) Morosan, E.; Zandbergen, H. W.; Dennis, B. S.; Bos, J. W. G.; Onose, Y.; Klimczuk, T.; Ramirez, A. P.; Ong, N. P.; Cava, R. J. Superconductivity in Cu<sub>x</sub>TiSe<sub>2</sub>. *Nat. Phys.* **2006**, *2*, 544–550.
- (9) Yao, J.; Koski, K. J.; Luo, W. D.; Cha, J. J.; Hu, L. B.; Kong, D. S.; Narasimhan, V. K.; Huo, K. F.; Cui, Y. Optical transmission enhancement through chemically tuned two-dimensional bismuth chalcogenide nanoplates. *Nat. Commun.* **2014**, *5*, 5670.
- (10) Chen, S.; Johnson, V. L.; Donadio, D.; Koski, K. J. Mn-intercalated MoSe<sub>2</sub> under pressure: Electronic structure and vibrational characterization of a dilute magnetic semiconductor. *J. Chem. Phys.* **2020**, *153*, No. 124701.
- (11) Xiong, F.; Wang, H.; Liu, X.; Sun, J.; Brongersma, M.; Pop, E.; Cui, Y. Li Intercalation in  $MoS_2$ : In Situ Observation of Its Dynamics and Tuning Optical and Electrical Properties. *Nano Lett.* **2015**, *15*, 6777–6784.
- (12) Husremovic, S.; Groschner, C. K.; Inzani, K.; Craig, I. M.; Bustillo, K. C.; Ercius, P.; Kazmierczak, N. P.; Syndikus, J.; Van Winkle, M.; Aloni, S.; Taniguchi, T.; Watanabe, K.; Griffin, S. M.; Bediako, D. K. Hard Ferromagnetism Down to the Thinnest Limit of Iron-Intercalated Tantalum Disulfide. *J. Am. Chem. Soc.* **2022**, *144*, 12167–12176.
- (13) Disalvo, F. J.; Hull, G. W.; Schwartz, L. H.; Voorhoeve, J. M.; Waszczak, J. V. Metal Intercalation Compounds of TaS<sub>2</sub> Preparation and Properties. *J. Chem. Phys.* **1973**, *59*, 1922–1929.
- (14) Wu, Y.; Li, D.; Wu, C.-L.; Hwang, H. Y.; Cui, Y. Electrostatic gating and intercalation in 2D materials. *Nat. Rev. Mater.* **2023**, *8*, 41–53.
- (15) Zhou, J.; Lin, Z.; Ren, H.; Duan, X.; Shakir, I.; Huang, Y.; Duan, X. Layered Intercalation Materials. *Adv. Mater.* **2021**, 33, No. 2004557.
- (16) Chen, H. W.; Ma, H. Y.; Li, C. Host-Guest Intercalation Chemistry in MXenes and Its Implications for Practical Applications. *ACS Nano* **2021**, *15*, 15502–15537.
- (17) Chhowalla, M.; Shin, H. S.; Eda, G.; Li, L. J.; Loh, K. P.; Zhang, H. The chemistry of two-dimensional layered transition metal dichalcogenide nanosheets. *Nat. Chem.* **2013**, *5*, 263–275.
- (18) Wang, Q. H.; Kalantar-Zadeh, K.; Kis, A.; Coleman, J. N.; Strano, M. S. Electronics and optoelectronics of two-dimensional transition metal dichalcogenides. *Nat. Nanotechnol.* **2012**, *7*, 699–712.
- (19) Ding, H. M.; Li, Y. B.; Li, M.; Chen, K.; Liang, K.; Chen, G. X.; Lu, J.; Palisaitis, J.; Persson, P. O. A.; Eklund, P.; Hultman, L.; Du, S. Y.; Chai, Z. F.; Gogotsi, Y.; Huang, Q. Chemical scissor-mediated structural editing of layered transition metal carbides. *Science* 2023, 379, 1130–1135.
- (20) Motter, J. P.; Koski, K. J.; Cui, Y. General Strategy for Zero-Valent Intercalation into Two-Dimensional Layered Nanomaterials. *Chem. Mater.* **2014**, *26*, 2313–2317.
- (21) Koski, K. J.; Wessells, C. D.; Reed, B. W.; Cha, J. J.; Kong, D.; Cui, Y. Chemical intercalation of zerovalent metals into 2D layered Bi<sub>2</sub>Se<sub>3</sub> nanoribbons. *J. Am. Chem. Soc.* **2012**, *134*, 13773–13779.
- (22) Xie, L. S.; Husremović, S.; Gonzalez, O.; Craig, I. M.; Bediako, D. K. Structure and Magnetism of Iron- and Chromium-Intercalated Niobium and Tantalum Disulfides. *J. Am. Chem. Soc.* **2022**, *144*, 9525–9542.
- (23) Koski, K. J.; Cha, J. J.; Reed, B. W.; Wessells, C. D.; Kong, D. S.; Cui, Y. High-Density Chemical Intercalation of Zero-Valent Copper into Bi<sub>2</sub>Se<sub>3</sub> Nanoribbons. *J. Am. Chem. Soc.* **2012**, *134*, 7584–7587.
- (24) He, Q.; Lin, Z.; Ding, M.; Yin, A.; Halim, U.; Wang, C.; Liu, Y.; Cheng, H. C.; Huang, Y.; Duan, X. In Situ Probing Molecular Intercalation in Two-Dimensional Layered Semiconductors. *Nano Lett.* **2019**, *19*, *6819*–*6826*.

- (25) Wang, C.; He, Q.; Halim, U.; Liu, Y.; Zhu, E.; Lin, Z.; Xiao, H.; Duan, X.; Feng, Z.; Cheng, R.; Weiss, N. O.; Ye, G.; Huang, Y. C.; Wu, H.; Cheng, H. C.; Shakir, I.; Liao, L.; Chen, X.; Goddard, W. A.; Huang, Y.; Duan, X. Monolayer atomic crystal molecular superlattices. *Nature* **2018**, *555*, 231–236.
- (26) Schmidt, H.; Giustiniano, F.; Eda, G. Electronic transport properties of transition metal dichalcogenide field-effect devices: surface and interface effects. *Chem. Soc. Rev.* **2015**, *44*, 7715–7736.
- (27) Marseglia, E. A. Transition metal dichalcogenides and their intercalates. *Int. Rev. Phys. Chem.* **1983**, *3*, 177–216.
- (28) Whittingham, M. S. Chemistry of intercalation compounds: Metal guests in chalcogenide hosts. *Prog. Solid State Chem.* 1978, 12, 41–99
- (29) Tsai, H.-l.; Heising, J.; Schindler, J. L.; Kannewurf, C. R.; Kanatzidis, M. G. Exfoliated-Restacked Phase of WS<sub>2</sub>. *Chem. Mater.* **1997**, 9, 879–882.
- (30) Heising, J.; Kanatzidis, M. G. Exfoliated and restacked MoS<sub>2</sub> and WS<sub>2</sub>: Ionic or neutral species? Encapsulation and ordering of hard electropositive cations. *J. Am. Chem. Soc.* **1999**, *121*, 11720–11732.
- (31) Kuo, D. Y.; Cossairt, B. M. Direct intercalation of MoS<sub>2</sub> and WS<sub>2</sub> thin films by vacuum filtration. *Mater. Horiz.* **2022**, *9*, 360–367.
- (32) Kuo, D. Y.; Rice, P. S.; Raugei, S.; Cossairt, B. M. Charge Transfer in Metallocene Intercalated Transition Metal Dichalcogenides. *J. Phys. Chem. C* **2022**, *126*, 13994–14002.
- (33) Bae, S.; Matsumoto, K.; Raebiger, H.; Shudo, K.-i.; Kim, Y.-H.; Handegård, Ø. S.; Nagao, T.; Kitajima, M.; Sakai, Y.; Zhang, X.; Vajtai, R.; Ajayan, P.; Kono, J.; Takeda, J.; Katayama, I. K-point longitudinal acoustic phonons are responsible for ultrafast intervalley scattering in monolayer MoSe<sub>2</sub>. *Nat. Commun.* **2022**, *13*, 4279.
- (34) Xu, B. H.; Lin, B. Z.; Chen, Z. J.; Li, X. L.; Wang, Q. Q. Preparation and electrical conductivity of polypyrrole/WS<sub>2</sub> layered nanocomposites. *J. Colloid Interface Sci.* **2009**, 330, 220–226.
- (35) Zhu, K. X.; Tao, Y. Y.; Clark, D. E.; Hong, W.; Li, C. W. Solution-Phase Synthesis of Vanadium Intercalated 1T'-WS<sub>2</sub> with Tunable Electronic Properties. *Nano Lett.* **2023**, 23, 4471–4478.
- (36) Luo, Y.; Li, X.; Cai, X.; Zou, X.; Kang, F.; Cheng, H. M.; Liu, B. Two-Dimensional MoS<sub>2</sub> Confined Co(OH)<sub>2</sub> Electrocatalysts for Hydrogen Evolution in Alkaline Electrolytes. *ACS Nano* **2018**, *12*, 4565–4573.
- (37) Chen, Z.; Leng, K.; Zhao, X.; Malkhandi, S.; Tang, W.; Tian, B.; Dong, L.; Zheng, L.; Lin, M.; Yeo, B. S.; Loh, K. P. Interface confined hydrogen evolution reaction in zero valent metal nanoparticles-intercalated molybdenum disulfide. *Nat. Commun.* **2017**, *8*, 14548.
- (38) Yang, D.; Frindt, R. F. Li-intercalation and exfoliation of WS<sub>2</sub>. *J. Phys. Chem. Solids* **1996**, *57*, 1113–1116.
- (39) Ravel, B.; Newville, M. ATHENA, ARTEMIS, HEPHAESTUS: data analysis for X-ray absorption spectroscopy using IFEFFIT. *J. Synchrotron Radiat.* **2005**, *12*, 537–541.
- (40) Melitz, W.; Shen, J.; Kummel, A. C.; Lee, S. Kelvin probe force microscopy and its application. *Surf. Sci. Rep.* **2011**, *66*, 1–27.
- (41) Nonnenmacher, M.; O'Boyle, M. P.; Wickramasinghe, H. K. Kelvin Probe Force Microscopy. *Appl. Phys. Lett.* **1991**, *58*, 2921–2923.
- (42) Filleter, T.; Emtsev, K. V.; Seyller, T.; Bennewitz, R. Local work function measurements of epitaxial graphene. *Appl. Phys. Lett.* **2008**, 93, No. 133117.
- (43) Lee, N. J.; Yoo, J. W.; Choi, Y. J.; Kang, C. J.; Jeon, D. Y.; Kim, D. C.; Seo, S.; Chung, H. J. The interlayer screening effect of graphene sheets investigated by Kelvin probe force microscopy. *Appl. Phys. Lett.* **2009**, *95*, No. 222107.
- (44) Chwang, R.; Smith, B. J.; Crowell, C. R. Contact size effects on the van der Pauw method for resistivity and Hall coefficient measurement. *Solid-State Electron.* **1974**, *17*, 1217–1227.
- (45) Ramadan, A. A.; Gould, R. D.; Ashour, A. On the Van der Pauw method of resistivity measurements. *Thin Solid Films* **1994**, 239, 272–275.
- (46) Persson, I. Hydrated metal ions in aqueous solution: How regular are their structures? *Pure Appl. Chem.* **2010**, 82, 1901–1917.

- (47) Shannon, R. D. Revised Effective Ionic-Radii and Systematic Studies of Interatomic Distances in Halides and Chalcogenides. *Acta Crystallogr. A* **1976**, 32, 751–767.
- (48) CRC Handbook of Chemistry and Physics; 95th ed.; Haynes, W. M., Ed.; CRC Press: Boca Raton, FL, 2004, pp 5-80-5-89.
- (49) Han, J. H.; Kim, H. K.; Baek, B.; Han, J.; Ahn, H. S.; Baik, M. H.; Cheon, J. Activation of the Basal Plane in Two Dimensional Transition Metal Chalcogenide Nanostructures. *J. Am. Chem. Soc.* **2018**, *140*, 13663–13671.
- (50) Acerce, M.; Voiry, D.; Chhowalla, M. Metallic 1T phase MoS<sub>2</sub> nanosheets as supercapacitor electrode materials. *Nat. Nanotechnol.* **2015**, *10*, 313–318.
- (51) Wang, M.; Williams, D.; Lahti, G.; Teshima, S.; Dominguez Aguilar, D.; Perry, R.; Koski, K. J Chemical intercalation of heavy metal, semimetal, and semiconductor atoms into 2D layered chalcogenides. 2D Mater. 2018, 5, No. 045005.
- (52) Reed, B. W.; Tran, C.; Koski, K. J. Brillouin scattering of zero-valent Au-, Cu-, Ag-intercalated hexagonal boron nitride. *Phys. Rev. Mater.* **2023**, *7*, No. 044003.
- (53) Chen, K. P.; Chung, F. R.; Wang, M. J.; Koski, K. J. Dual Element Intercalation into 2D Layered Bi<sub>2</sub>Se<sub>3</sub> Nanoribbons. *J. Am. Chem. Soc.* **2015**, *137*, 5431–5437.
- (54) Wang, M. J.; Koski, K. J. Reversible Chemochromic MoO<sub>3</sub> Nanoribbons through Zerovalent Metal Intercalation. *ACS Nano* **2015**, *9*, 3226–3233.
- (55) Shuai, J.; Yoo, H. D.; Liang, Y. L.; Li, Y. F.; Yao, Y.; Grabow, L. C. Density functional theory study of Li, Na, and Mg intercalation and diffusion in MoS<sub>2</sub> with controlled interlayer spacing. *Mater. Res. Express* **2016**, *3*, No. 064001.
- (56) Muldoon, J.; Bucur, C. B.; Gregory, T. Quest for Nonaqueous Multivalent Secondary Batteries: Magnesium and Beyond. *Chem. Rev.* **2014**, *114*, 11683–11720.
- (57) Levi, M. D.; Lancry, E.; Gizbar, H.; Lu, Z.; Levi, E.; Gofer, Y.; Aurbach, D. Kinetic and thermodynamic studies of  $Mg^{2+}$  and Li<sup>+</sup> ion insertion into the  $Mo_6S_8$  Chevrel phase. *J. Electrochem. Soc.* **2004**, *151*, A1044–A1051.
- (58) Levi, E.; Gofer, Y.; Aurbach, D. On the Way to Rechargeable Mg Batteries: The Challenge of New Cathode Materials. *Chem. Mater.* **2010**, 22, 860–868.
- (59) Aurbach, D.; Suresh, G. S.; Levi, E.; Mitelman, A.; Mizrahi, O.; Chusid, O.; Brunelli, M. Progress in rechargeable magnesium battery technology. *Adv. Mater.* **2007**, *19*, 4260–4267.
- (60) Amir, N.; Vestfrid, Y.; Chusid, O.; Gofer, Y.; Aurbach, D. Progress in nonaqueous magnesium electrochemistry. *J. Power Sources* **2007**, *174*, 1234–1240.
- (61) Suresh, G. S.; Levi, M. D.; Aurbach, D. Effect of chalcogen substitution in mixed  $Mo_6S_{8-n}Se_n$  (n = 0, 1, 2) Chevrel phases on the thermodynamics and kinetics of reversible Mg ions insertion. *Electrochim. Acta* **2008**, 53, 3889–3896.
- (62) Zhu, J.; Zeng, Z. H.; Li, W. X. K-Edge XANES Investigation of Fe-Based Oxides by Density Functional Theory Calculations. *J. Phys. Chem. C* **2021**, *125*, 26229–26239.
- (63) Kumar, D.; Singh, B.; Kumar, P.; Balakrishnan, V.; Kumar, P. Thermal expansion coefficient and phonon dynamics in coexisting allotropes of monolayer WS<sub>2</sub> probed by Raman scattering. *J. Phys.: Condens. Matter* **2019**, *31*, No. 505403.
- (64) Calandra, M. Chemically exfoliated single-layer MoS<sub>2</sub>: Stability, lattice dynamics, and catalytic adsorption from first principles. *Phys. Rev. B* **2013**, 88, No. 245428.